Journal of ELECTRONIC MATERIALS, Vol. 49, No. 9, 2020
https://doi.org/10.1007/s11664-020-08260-1
© 2020 The Author(s)

TOPICAL COLLECTION: 18TH CONFERENCE ON DEFECTS (DRIP XVIII)

Vacancy Clustering in Dislocation-Free High-Purity Germanium

KEVIN-PETER GRADWOHL,[1] ALEXANDER GYBIN,[1]
JÓZSEF JANICSKÓ-CSÁTHY,[1] MELISSA RODER,[2]
ANDREAS N. DANILEWSKY,[2] and R. RADHAKRISHNAN SUMATHI[1,3]

1.—Leibniz-Institut für Kristallzüchtung (IKZ), Max-Born-Str. 2, 12489 Berlin, Germany. 2.—Kristallographie, Albert-Ludwigs-Universität Freiburg, Hermann-Herder-Str. 5, 79104 Freiburg, Germany. 3.—e-mail: radhakrishnan.sumathi@ikz-berlin.de

A germanium crystal of high purity was grown in H_2 with a maximum dislocation density of 3000 cm^{-2}, which was estimated by white beam x-ray topography. Due to a dynamical diffraction effect, the topographs revealed the existence of vacancy clusters in the form of voids in dislocation-free parts of the crystal. Etch pit density analysis, the standard technique employed for crystalline wafers to determine dislocation density, failed to reliably represent dislocations in dislocation-free parts of the crystal. On the other hand, we were able to identify a different type of etching pattern for a dislocation-free crystal. Microwave photoconductance decay was utilized to determine the charge carrier lifetime, which was found to be up to 500 μs for regions with dislocations, while being only 100 μs for dislocation-free parts of the crystal.

Key words: High-purity germanium, dislocations, vacancies, voids, crystal growth

INTRODUCTION

High-purity germanium (HPGe) plays a key role as detector material for high-resolution gamma-ray detectors. Recent interest in HPGe is motivated by the needs of the large enriched germanium experiment for neutrinoless double-beta decay (LEGEND) built for the search for the neutrinoless double-beta decay of ^{76}Ge using one ton of HPGe detectors.[1] Since the next generation of detectors for the LEGEND experiment require large mass detectors, the Ge crystals have to be of exceptional quality. They require ultrahigh purity, i.e. a net charge carrier density $< 10^{10}$ cm^{-3}, to be fully depleted. Furthermore, the lifetime has to be much larger than the drift time of the carriers in the detector. A large charge carrier mobility lifetime product of < 1 cm^2/V is required. For typical electron mobility of single-crystalline HPGe in liquid nitrogen (77 K) of 40000 cm^2 V^{-1} s^{-1}, this results in charge carrier lifetime much higher than 25 μs. These high lifetimes can only be acquired by ensuring a low density of structural defects such as dislocations and voids. However, completely dislocation-free Ge is unfavorable, since there the vacancies dominate the defect landscape, resulting in vacancy-related complexes such as V_2H[2,3] and vacancy clusters in the form of voids,[4] rendering the material worthless for detector applications. At the melting point, the concentration of vacancies is somewhere between 10^{14} cm^{-3} and 10^{15} cm^{-3}, while the concentration of self-interstitials is only 10^9 cm^{-3}.[5,6] Therefore, the Frank–Turnbull reaction $V_{Ge} + Ge_i \leftrightarrow Ge_{Ge}$ is not sufficient to annihilate the vacancies during the crystal cooling process.[7] The presence of dislocations with edge character would allow the vacancies to be fixed around the dislocation lines, typically known as dislocation decoration, and act as an effective sink for vacancies. In the case of almost no dislocations, the vacancies ultimately have to cluster.[4] Hence, it is preferred to have a dislocation density between 10^2 cm^{-2} and 10^4 cm^{-2}. By controlling the temperature gradient during crystal growth, the distribution of

(Received February 17, 2020; accepted June 9, 2020; published online June 30, 2020)

dislocation density can be controlled to a certain degree to fulfill the detector requirements.[8,9] It is of crucial importance to be able to reliably determine the concentration of structural defects inside the crystal. For this purpose, we demonstrate that etch pit density analysis is not always reliable for determining dislocation density for crystals with low dislocation density or close to zero dislocations. It was possible to prove this by utilizing complementary white beam x-ray topography measurements to show the actual dislocation density as well as the presence of voids in dislocation-free parts of the crystal. We were also able to show that the etching figure of dislocation-free Ge can be differentiated from dislocated Ge, where etch pits represent dislocation lines cutting the surface. The charge carrier lifetime was significantly lower in the dislocation-free part, on average below 100 μs, which is not sufficient for large Ge detectors. Beyond, the material had sufficient carrier lifetime up to 500 μs in the dislocated parts.

EXPERIMENTAL

Crystal Growth

A Ge single crystal with a diameter of 2 inches was grown in a H_2 atmosphere by the Czochralski method from a [0 0 1]-oriented crystal seed fabricated from a high-quality Ge crystal (Fig. 1). The Ge material for crystal growth was purified in a zone refining process, which is described elsewhere in detail, together with the exact growth setup.[10] The crystal was grown from a 4-inch fused silica crucible within a custom-built crystal growth setup. The hot-zone and growth conditions were optimized by continuous experimental investigation of the crystals and numerical simulations, as shown in the work of Miller et al.[11]. In particular, the shape of the melt/crystal interface was optimized by adjusting crystal growth parameters to reduce thermal stress, and consequently dislocation multiplication, during crystal growth, which was necessary to control the dislocation density of the grown crystal. For characterization and investigation of the crystal, three (0 0 1) wafers were cut along the crystal length, which were oriented within an angular tolerance < 1°. The three wafers, referred to as A (top), B (middle) and C (tail) portions of the grown crystals, are depicted in Fig. 1, and have thicknesses of 700, 800 μm and 350, respectively. For various investigations the wafers were chemo-mechanically polished on both sides.

White Beam X-ray Topography

White beam x-ray topography was performed at the Karlsruhe Research Accelerator (KARA) synchrotron of Karlsruhe Institute of Technology (KIT). This is a synchrotron with a 2.5 GeV electron storage ring. The measurements were conducted at the topography station at the imaging cluster of the KIT light source, which is described in detail elsewhere.[12] The topographs were recorded with Slavich VRP-M high-resolution photographic film and a two-dimensional indirect detector with a pixel size of 2.5 μm. The Ge samples were measured in transmission geometry with a distance between film/detector and samples of 90 mm and with several minutes of exposure time. The beam size at the sample was approximately 8 mm × 5 mm. The horizontal axis of the wafers was the [1 1 0] axis, and the samples were tilted around this axis by 14° and by 28°, to reach the $2\bar{2}0$ and the $1\bar{3}\bar{1}$ Bragg reflection, respectively. The reflections of the Laue patterns were identified using LauePt software.[13]

Microwave Photoconductance Decay

The bulk carrier lifetime τ was determined by microwave photoconductance decay (μ-PCD) using MDPmap, a commercially available tool from Freiberg Instruments. The setup consists of a laser mounted next to a microwave spectrometer above the sample and a microwave cavity beneath the sample table. The sample table is freely rotatable and movable for lateral scanning. The details of the experimental setup are explained elsewhere.[14] The main advantage of this technique is the ability to measure the carrier lifetime in a contactless manner and without fabrication of electrical contacts. The measurement principle is based on the change in microwave reflectivity as a function of excess carrier concentration, which is initially generated by a laser.[15–17] After illumination, the decay of the excess carrier concentration is approximated with a single exponential fit to obtain the carrier lifetime from its exponent coefficient −1/

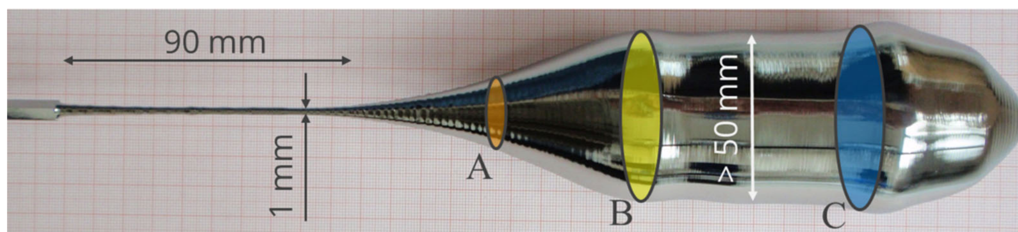

Fig. 1. A [0 0 1] Ge single crystal grown in H_2 with a diameter well above 2 inches. The seed of the crystal can be seen on the left side, followed by a long and thin Dash neck. For further investigation and characterization, three wafers were cut from the crystal, which are denoted by A, B, and C.

τ, which is valid if the lifetime is independent of the carrier density. Hence, the bulk carrier lifetime is measured by the decay of the excess carrier density, which is sufficient if surface recombination does not significantly affect the change in carrier density and consequently the microwave reflectivity. This was ensured by preparing the wafers by chemo-mechanical polishing on both sides to eliminate any surface defects originating from cutting and polishing. The wafers were measured under ambient conditions at 22°C. Two different lasers were tested, a near-infrared laser with a wavelength of 980 nm and a red laser with 660 nm wavelength. The laser power was modulated between 20 and 100 mW and 10–30 mW for the near-infrared and the red laser, respectively. The most stable results were obtained by the 980 nm near-infrared laser at power of 80 mW, which was utilized for all presented μ-PCD measurements. However, it should be should mentioned that the laser power and wavelength had no noteworthy impact on the average lifetime. For every measurement, laser illumination was carried out for 1000 ms to ensure complete saturation, and for every spot on the wafer an average over ten independent measurements was performed. The laser can be focused to a spot size with a diameter of approximately 0.5 mm; therefore, a measurement step size of 0.2 mm was chosen to ensure slight oversampling.

Etching

An etch pit density (EPD) analysis was conducted to investigate the dislocation density, since dislocation cores can be the preferred etching sites. The surfaces have to be of low roughness and without a major defect layer. This is achieved by grinding/lapping the wafers with SiC abrasive, followed by a chemo-mechanical polishing procedure. The etching solution was a modified CP-4 etch. The wafers were submerged into the acid in a Teflon vessel at 22°C. A large amount of acid relative to the volume of the wafers ($\approx$ 800 ml acid) was used to avoid significant warming of the etching solution. After 60 min, the etchant was replaced by deionized water with resistivity of 17–18 MΩ cm. The etched wafers were then investigated by differential interference contrast microscopy. The EPD values were determined by counting the large faceted etch pits originating from the dislocation cores and dividing their number by the investigated area.

RESULTS AND DISCUSSION

The HPGe crystal was grown from a [0 0 1] HPGe seed with a 5 $\times$ 5 mm^2 cross section.[10] To control the initial dislocations, the Dash-necking technique[18] was used, growing a neck 90 mm long and down to 1 mm thin at high growth speed, as shown in Fig. 1. Within the crystal shoulder the diameter was increased to 2 inches. The length of the crystal was 220 mm excluding the Dash neck and seed, resulting in a total crystal mass of 1.6 kg.

White Beam X-ray Topography

For the characterization of the structural defects, white beam x-ray topography in transmission geometry was conducted. Wafer A was investigated first with a low-resolution film, to determine the exact positions of the desired reflections and to obtain a first impression of the dislocation density. The investigated area in the middle of the wafer was free of dislocations in all reflections. Therefore, the $2\bar{2}0$ reflection was chosen for a wafer map, which was stitched together by topographs recorded on a two-dimensional detector. This reflection was chosen because it is reachable with a simple rotation around the horizontal [1 1 0] axis of the wafer, which makes it easy to correctly adjust the detector spatially.

A $2\bar{2}0$ x-ray topograph of wafer A is shown in Fig. 2. The growth ridges can be seen on the wafer edge, which originate from the thermodynamic dominance of the {1 1 1} facets in Ge during crystal growth. The wafer is mostly free of dislocations. Only a few dislocations can be identified, which are highlighted by arrows, which also indicate their crystallographic direction. The total dislocation density of wafer A was calculated from the length of the dislocations divided by the wafer volume (wafer thickness 700 μm) and was found to be below 1 cm^{-2}. It should be mentioned that the dislocations seem to be located in the edge regions of the wafer. This is most likely explained by a completely dislocation-free crystal shortly after the Dash neck, and new dislocations originating from the surface of the crystal during growth. A region in the order of 1 cm^2 in the wafer center was completely dislocation-free. Voids can also be observed on the wafer, which are visible due to a black–white contrast following the diffraction vector. The voids originate from vacancy clustering during crystal growth,

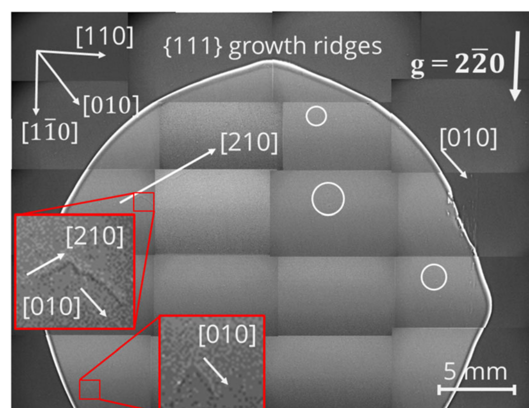

Fig. 2. $2\bar{2}0$ X-ray topograph of A with the dislocations marked by white arrows, indicating their crystallographic orientations. The red insets show dislocations in detail. The total dislocation density throughout the wafer was found to be below 1 cm^{-2}. The white circles indicate the positions of voids on the wafer (Color figure online).

since in Ge the dominant intrinsic defects are vacancies and not self-interstitials. The voids are highlighted in the image by white circles in Fig. 2 and can be seen in detail in Fig. 3.

The void is indicated in the center of the figure by the black–white contrast following the diffraction vector, which is caused by a dynamical diffraction effect. The dynamical theory can be applied since the perfection of the crystal is very high, namely due to high chemical purity, no grain boundaries and no dislocations.[19–22] It is based on the change in diffraction intensity due to a shift of the tie points of the wave fields on the hyperbolic dispersion surface, caused by the elastic deformations around the void. A more detailed explanation can be found elsewhere, where the effect was observed experimentally and theoretically in silicon.[23–25]

Several such voids were detected throughout the crystal. It should be mentioned that this method is only sensitive to voids close to the exit surface of the sample. This is due to the sensitivity of the effective absorption coefficient for anomalous transmission on deviations from the exact Bragg condition. Therefore, it is not trivial to estimate the void density from the experimental investigations. Simply dividing the number of observed voids (black–white contrasts) by the volume of the whole wafer would always underestimate the present void density n_{void}; for the wafer map it would yield a void density of 10 cm^{-3}, which is not realistic. This can be shown by an estimation of the void density by thermodynamic considerations. A vacancy density n_{V} at the melting point of Ge of 10^{14} cm^{-3} is assumed,[5,6] and we further assume that all of these vacancies are able to condense into spherical voids, which are well separated from each other, i.e. no overlapping. The void density can then be estimated by:

$$n_{\mathrm{void}} \approx \frac{n_{\mathrm{V}}}{n_{\mathrm{Ge}}} \cdot d^{-3},$$

where n_{Ge} is the number of Ge atoms per cm^3—which is 4×10^{23} cm^{-3} at the melting point—and d is the diameter of the void. If we estimate the void density based on the experimental observation as calculated before, but correct such that the technique is only sensitive to voids close to the exit surface, where close means in the order of the size of the void d, the observed void density is then obtained as $n_{\mathrm{void}} \approx 10\ \mathrm{cm}^{-2}\ \mathrm{d}^{-1}$. These two relations yield the same void density of 10^5 cm^{-3} for voids of 100 nm diameter. This makes it a challenging task to find direct evidence of voids by any means of microscopy. Hens et al.[26] reported the simulation of void distribution for Ge crystals resulting from vacancy clusters of 1–6 μm. Large crystallographic pits (similar to crystal-originated particles (COPs) in Si) on polished Ge wafers were occasionally identified by optical microscopy, and these observed surface pits were assigned as voids.

As stated before, this clustering of vacancies only occurs due to a lack of vacancy-absorbing mechanisms in dislocation-free crystals. Consequently, in crystals with moderate dislocation density, one would always expect dislocation climb to be a sufficient mechanism to avoid clustering of vacancies into voids. A $1\bar{3}\bar{1}$ topograph of wafer C (crystal tail) is shown in Fig. 4. The most striking feature is the network of dislocations, which are polygonized, more or less regular full and half hexagons. The straight dislocation lines strictly follow the $<1\ 1\ 0>$ directions of the crystal, due to the high Peierls potential in Ge. The dislocation density was found to be about 3000 cm^{-2}, which was again determined by dividing the total dislocation length by the measurement volume. The formation of dislocation bundles can be partially observed, but in most cases the dislocations are several hundred micrometers in length and undisturbed. The small black dots are defects in the film, and the vertical black line in the left part of the image is a scratch in the film. There is no evident indication of voids, as expected. Generally, in the areas with moderate dislocation density, no voids could be observed.

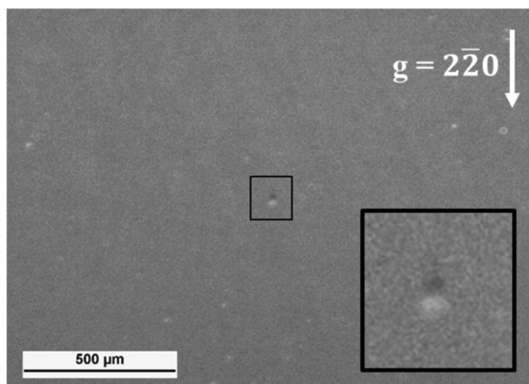

Fig. 3. $2\bar{2}0$ x-ray topograph of wafer A without any dislocations and the black–white contrast, which is caused by a dynamical diffraction effect.

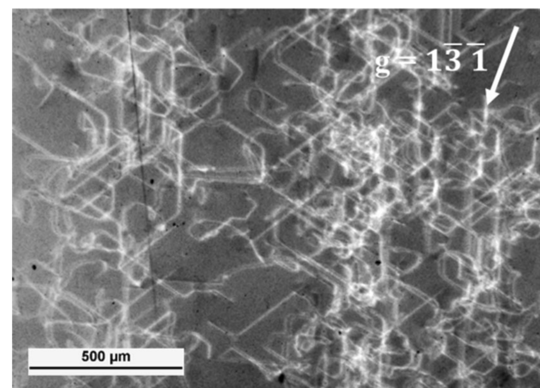

Fig. 4. $1\bar{3}\bar{1}$ x-ray topograph of wafer C depicting a dislocation network with pseudo-hexagonal loops and a moderate dislocation density of 3000 cm^{-2}. No voids can be observed in parts of the crystal with moderate dislocation density.

Microwave Photoconductance Decay

Spatially resolved μ-PCD measurements were carried out to obtain the bulk lifetime maps depicted in Fig. 5 for the three wafers A, B, and C at the positions indicated in Fig. 1. Most remarkable are the differences in average lifetime between the three wafers, which is represented by a common color scale on the side of Fig. 5. The average lifetime $\bar{\tau}$ increases along the crystal length: while it is only 83 μs at the very top of the crystal (wafer A), it increases to 285 μs for wafer B and finally reaches 423 μs at the crystal tail (wafer C). A comparison with the x-ray topography results shows that wafer A from the neck portion of the crystal with the lowest dislocation density has a low charge carrier lifetime, while wafer C before the tail portion of the crystal having homogeneously distributed dislocations with a density of 3000 cm^{-2} exhibits a high charge carrier lifetime. This unequivocal result merits further detailed measurement investigations in correlation with the dislocations and also with respect to voids observed in the x-ray topograph of wafer A in Fig. 2. Although the lifetime measurement was done at room temperature, it is fully consistent with the results obtained by Sande et al.[27] with HPGe detectors. The reduced lifetime of wafer A may be due to vacancy-related recombination centers, as the voids alone cannot explain an influence on the lifetime. Furthermore, a certain inhomogeneity within the lifetime maps of the wafers can be observed, especially in wafer A and B. However, this inhomogeneity could not be directly correlated with the dislocations/voids observed in the x-ray topograph of A in Fig. 2. Locally, the lifetime on wafer A drops below 20 μs. Wafer B exhibits the greatest non-uniformity in lifetime, which we attribute to the transition between dislocation-free and dislocated parts of the crystal. Wafer C shows the required lifetime values for detector applications over the entire wafer surface.

Etching

In order to gain insight into the defect density and uniformity of the crystal, an EPD analysis was carried out. The etched wafers were investigated by differential interference contrast microscopy, which can be seen in Fig. 6. All the wafers clearly exhibit etch pits after etching. On all three wafers, the large etch pits are composed of {1 1 1} facets (octahedral-shaped) with a rounded bottom. The calculated EPD values from a representative square-centimeter-sized area are shown in Fig. 7. The EPD values are 5000 cm^{-2} for A, 5700 cm^{-2} for B, and 3200 cm^{-2} for C. Only distinct faceted etch pits were taken into consideration for this value. Astonishingly, the dislocation-free wafer A has a high EPD value of 5000 cm^{-2}, where one would expect none. Wafer C has an EPD value of 3000 cm^{-2},

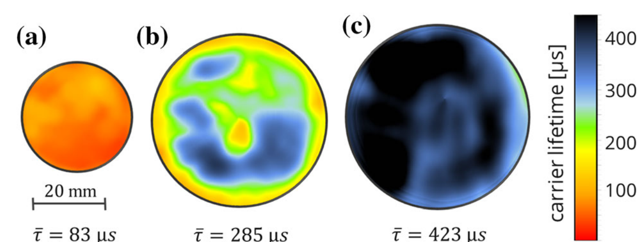

Fig. 5. μ-PCD bulk carrier lifetime maps for the wafers A, B, and C at the positions indicated in Fig. 1, with a common lifetime scale bar situated on the right.

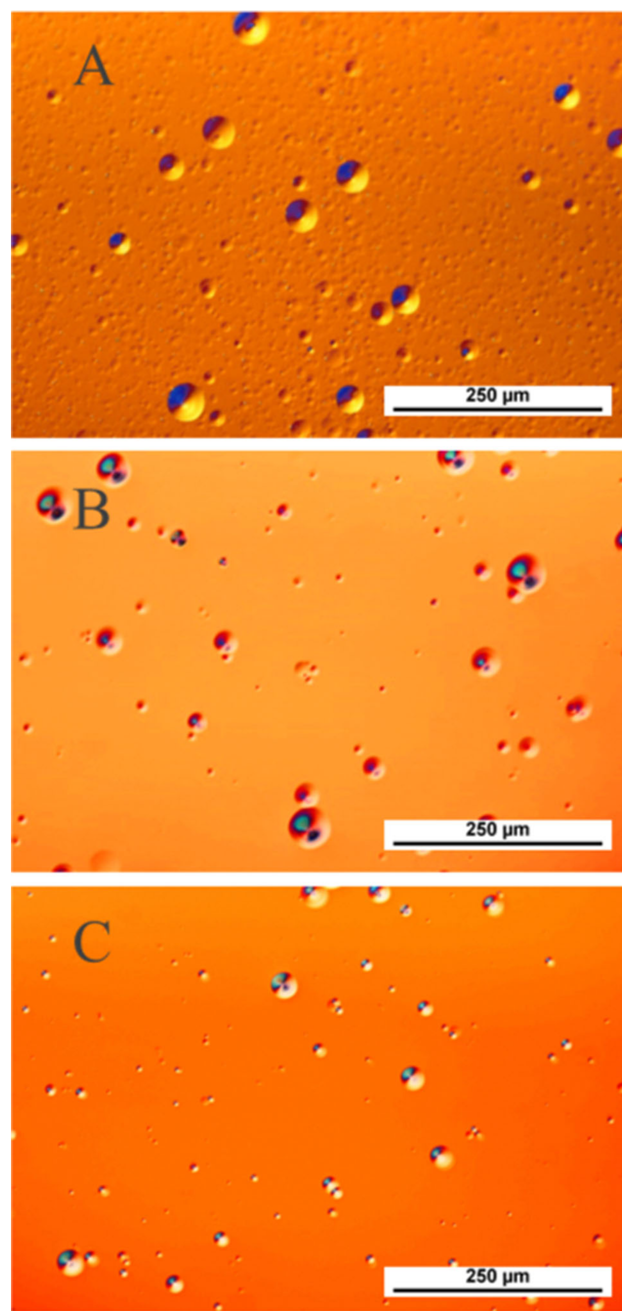

Fig. 6. Etching figure of the wafers A, B, and C in differential inference contrast microscopy. The large well-defined etch pits originate from dislocation cores. The dislocation-free wafer A shows a differentiated etch figure from the dislocated B and C wafer.

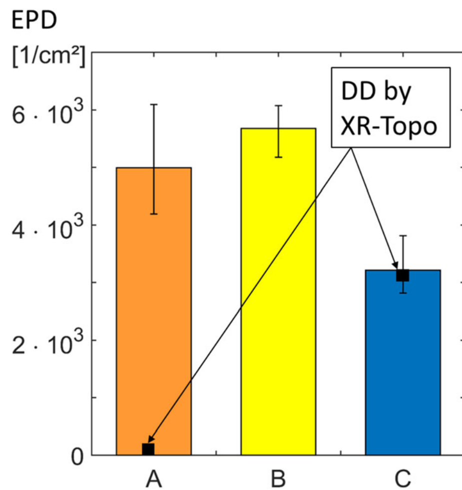

Fig. 7. The EPD values of the three wafers, determined on a representative square-centimeter-sized area by counting the large well-defined etch pits, were superimposed with the dislocation density observed in the x-ray topographs. The EPD value perfectly matches the dislocation density in wafer C, but does not represent dislocations of wafer A.

which matches very well with the value of the dislocation density estimated from x-ray topography. While the shape and the distribution of the etch pits looks similar in all parts of the crystal, wafer A shows a high density of "tiny" etch pits, which seem to be distributed over the entire sample surface. In wafers B and C, there are no such "tiny" etch pits, and the samples are completely smooth, as seen in the differential interference contrast (DIC) microscopy image, which suggests a roughness of only a few nanometers. In this regard, the vacancy clusters in the form of voids cannot be distinguished from etch pits arising from dislocations. The anticipated etch pit density for voids ($< 10\ cm^{-2}$) is far lower than the observed one. One may say that the tiny pits in sample A, which represent small prismatic dislocation loops, can form due to different preferred etch sites arising from vacancy condensation or vacancy-associated complexes rather than in parts of the crystal with moderate dislocation density, as in the case of samples B and C. Hence, it is possible to differentiate dislocation-free areas of the crystal with voids from parts with moderate dislocation density by observing the whole etch features.

CONCLUSIONS

Single-crystalline HPGe was grown under a H_2 atmosphere by the Czochralski technique using zone-refined material. The crystal was investigated in terms of structural defects by x-ray topography, more specifically in terms of dislocation distribution and formation of voids. The crystal grew initially completely free of dislocations ($< 1\ cm^{-2}$), due to dislocations growing out efficiently in the Dash neck. Towards the crystal tail, the dislocation density increased to $3000\ cm^{-2}$. The dislocations form straight-line hexagons, with the segments oriented in the $<1\ 1\ 0>$ directions. They are homogeneously distributed, which is good for detector applications. Furthermore, in parts of the crystal that are completely free of dislocations, the vacancies cluster into voids, which could be observed by a dynamical diffraction effect. The related void density is estimated to be $10^5\ cm^{-3}$, with an approximate void diameter of 100 nm. Dislocation density in HPGe was characterized by EPD analysis using a CP-4 etchant. However, it was possible to show by comparison to x-ray topographs that the observed EPD values do not represent the dislocation density in parts of the crystal where the dislocation density is close to zero. On the other hand, in wafer C, with moderate dislocation density, the EPD value corroborates the dislocation density observed by x-ray topography. The etching patterns differ between the dislocation-free and the dislocation-containing parts of the crystal, but the characteristic octahedral pits do not allow us to unambiguously distinguish the features from voids and dislocation-related etching. Tiny pits can be observed all over wafer A, while in wafer B and C the sample surface is almost smooth, as seen by DIC microscopy. This may be an indicator that wafer A is dislocation-free and dominated by V-related defects. The lifetimes measured by MPD decay reached average values above 250 μs throughout the bulk crystal, which is sufficient for detector applications. Additionally, the lifetime increased along the growth direction, which is inverse to the observed dislocation density. This can be explained by charge trapping based on vacancy-related defects.

ACKNOWLEDGMENTS

Open Access funding provided by Projekt DEAL. We thank the Karlsruhe Institute of Technology for the beam time at the Karlsruhe Research Accelerator synchrotron for investigation of our samples in the framework of the BIRD contract. We acknowledge the support of the German Federal Ministry for Education and Research (BMBF) within the collaborative project GERDA, under the Grant No.05A17BC1. The authors thank Dr. Uta Juda from the Leibniz-Institut für Kristallzüchtung for the support and help in the EPD analysis.

OPEN ACCESS

This article is licensed under a Creative Commons Attribution 4.0 International License, which permits use, sharing, adaptation, distribution and reproduction in any medium or format, as long as you give appropriate credit to the original author(s) and the source, provide a link to the Creative Commons licence, and indicate if changes were made. The images or other third party material in this article are included in the article's Creative Commons licence, unless indicated otherwise in a credit line to

the material. If material is not included in the article's Creative Commons licence and your intended use is not permitted by statutory regulation or exceeds the permitted use, you will need to obtain permission directly from the copyright holder. To view a copy of this licence, visit http://creativecommons.org/licenses/by/4.0/.

REFERENCES

1. N. Abgrall, A. Abramov, N. Abrosimov, I. Abt, M. Agostini, M. Agartioglu, A. Ajjaq, S. Alvis, F. Avignone III, X. Bai, M. Balata, I. Barabanov, A.S. Barabash, P.J. Barton, L. Baudis, L. Bezrukov, T. Bode, A. Bolozdynya, D. Borowicz, A. Boston, H. Boston, S.T.P. Boyd, R. Breier, V. Brudanin, R. Brugnera, M. Busch, M. Buuck, A. Caldwell, T.S. Caldwell, T. Camellato, M. Carpenter, C. Cattadori, J. Cederkäll, Y.-D. Chan, S. Chen, A. Chernogorov, C.D. Christofferson, P.-H. Chu, R.J. Cooper, C. Cuesta, E.V. Demidova, Z. Deng, M. Deniz, J.A. Detwiler, N. Di Marco, A. Domula, Q. Du, Yu. Efremenko, V. Egorov, S.R. Elliott, D. Fields, F. Fischer, A. Galindo-Uribarri, A. Gangapshev, A. Garfagnini, T. Gilliss, M. Giordano, G.K. Giovanetti, M. Gold, P. Golubev, C. Gooch, P. Grabmayr, M.P. Green, J. Gruszko, I.S. Guinn, V.E. Guiseppe, V. Gurentsov, Y. Gurov, K. Gusev, J. Hakenmüeller, L. Harkness-Brennan, Z. R. Harvey, C. R. Haufe, L. Hauertmann, D. Heglund, L. Hehn, A. Heinz, R. Hiller, J. Hinton, R. Hodak, W. Hofmann, S. Howard, M.A. Howe, M. Hult, L.V. Inzhechik, J. Janicskó Csáthy, R. Janssens, M. Ješkovský, J. Jochum, H.T. Johansson, D. Judson, M. Junker, J. Kaizer, K. Kang, V. Kazalov, Y. Kermadic, F. Kiessling, A. Kirsch, A. Kish, A. Klimenko, K.T. Knöpfle, O. Kochetov, S.I. Konovalov, I. Kontul, V.N. Kornoukhov, T. Kraetzschmar, K. Kröninger, A. Kumar, V.V. Kuzminov, K. Lang, M. Laubenstein, A. Lazzaro, Y. L. Li, Y.-Y. Li, H.B. Li, S.T. Lin, M. Lindner, I. Lippi, S.K. Liu, X. Liu, J. Liu, D. Loomba, A. Lubashevskiy, B. Lubsandorzhiev, G. Lutter, H. Ma, B. Majorovits, F. Mamedov, R.D. Martin, R. Massarczyk, J.A.J. Matthews, N. McFadden, D.-M. Mei, H. Mei, S.J. Meijer, D. Mengoni, S. Mertens, W. Miller, M. Miloradovic, R. Mingazheva, M. Misiaszek, P. Moseev, J. Myslik, I. Nemchenok, T. Nilsson, P. Nolan, C. O'Shaughnessy, G. Othman, K. Panas, L. Pandola, L. Papp, K. Pelczar, D. Peterson, W. Pettus, A.W.P. Poon, P.P. Povinec, A. Pullia, X.C. Quintana, D.C. Radford, J. Rager, C. Ransom, F. Recchia, A.L. Reine, S. Riboldi, K. Rielage, S. Rozov, N.W. Rouf, E. Rukhadze, N. Rumyantseva, R. Saakyan, E. Sala, F. Salamida, V. Sandukovsky, G. Savard, S. Schönert, A.-K. Schütz, O. Schulz, M. Schuster, B. Schwingenheuer, O. Selivanenko, B. Sevda, B. Shanks, E. Shevchik, M. Shirchenko, F. Simkovic, L. Singh, V. Singh, M. Skorokhvatov, K. Smolek, A. Smolnikov, A. Sonay, M. Spavorova, I. Stekl, D. Stukov, D. Tedeschi, J. Thompson, T. Van Wechel, R.L. Varner, A.A. Vasenko, S. Vasilyev, A. Veresnikova, K. Vetter, K. von Sturm, K. Vorren, M. Wagner, G.-J. Wang, D. Waters, W.-Z. Wei, T. Wester, B.R. White, C. Wiesinger, J.F. Wilkerson, M. Willers, C. Wiseman, M. Wojcik, H.T. Wong, J. Wyenberg, W. Xu, E. Yakushev, G. Yang, C.-H. Yu, Q. Yue, V. Yumatov, J. Zeman, Z. Zeng, I. Zhitnikov, B. Zhu, D. Zinatulina, A. Zschocke, A.J. Zsigmond, K. Zuber, and G. Zuzel, in *AIP Conference Proceedings* (2017) p. 020027.
2. E.E. Haller, W.L. Hansen, and F.S. Goulding, *Adv. Phys.* 30, 93 (1981).
3. I. Yonenaga, *Germanium Crystals: Single Crystals of Electronic Materials* (Sawston: Woodhead Publishing, 2019), pp. 89–127.
4. A.G. Tweet, *J. Appl. Phys.* 29, 1520 (1958).
5. J. Vanhellemont, P. Spiewak, and K. Sueoka, *J. Appl. Phys.* 101, 036103 (2007).
6. P. Spiewak, K. Sueoka, J. Vanhellemont, K. Kurzydlowski, K. Mlynarczyk, P. Wabinski, and I. Romandic, *Physica B* 401, 205 (2007).
7. F. Frank and D. Turnbull, *Phys. Rev.* 104, 617 (1956).
8. G. Wang, Y. Guan, H. Mei, D. Mei, G. Yang, J. Govani, and M. Khizar, *J. Cryst. Growth* 393, 54 (2014).
9. G. Wang, H. Mei, D. Mei, Y. Guan, and G. Yang, *J. Phys. Conf. Ser.* 606, 012012 (2015).
10. N. Abrosimov, M. Czupalla, N. Dropka, J. Fischer, A. Gybin, K. Irmscher, J. Janicsko-Csathy, U. Juda, S. Kayser, and W. Miller, *J. Cryst. Growth* 532, 125396 (2020).
11. W. Miller, N. Abrosimov, J. Fischer, A. Gybin, U. Juda, S. Kayser, and J. Janicsko-Csathy, *Crystals* 10, 18 (2020).
12. A. Rack, T. Weitkamp, S.B. Trabelsi, P. Modregger, A. Cecilia, T. dos Santos Rolo, T. Rack, D. Haas, R. Simon, and R. Heldele, *Nucl. Instrum. Methods Phys. Res. B Beam Interact. Mater. Atoms* 267, 978 (2009).
13. X. Huang, *J. Appl. Crystallogr.* 43, 926 (2010).
14. K. Dornich, Ph.D. thesis, TU Bergakademie Freiberg (2006).
15. G. Beck and M. Kunst, *Rev. Sci. Instrum.* 57, 197 (1986).
16. M. Kunst and G. Beck, *J. Appl. Phys.* 60, 3558 (1986).
17. K. Lauer, A. Laades, H. Ubensee, H. Metzner, and A. Lawerenz, *J. Appl. Phys.* 104, 104503 (2008).
18. W.C. Dash, *J. Appl. Phys.* 30, 459 (1959).
19. A. Authier and C. Malgrange, *Acta Crystallogr. A Found. Crystallogr.* 54, 806 (1998).
20. A. Authier, *International Tables for Crystallography* (Dordrecht: Springer, 2006), pp. 626–646.
21. B.K. Tanner, *X-ray diffraction topography*, Vol. 84 (Oxford: Pergamon Press, 1976).
22. P. Penning and D. Polder, *Philips Res. Rep* 16, 419 (1961).
23. T. Tuomi, R. Rantamaki, P. McNally, D. Lowney, A. Danilewsky, and P. Becker, *J. Phys. D Appl. Phys.* 34, A133 (2001).
24. R.D. Deslattes, E.G. Kessler Jr, S. Owens, D. Black, and A. Henins, *J. Phys. D Appl. Phys.* 32, A3 (1999).
25. A. Voloshin, I. Smolskii, V. Kaganer, V. Indenbom, and V. Rozhanskii, *Phys. Status Solidi A* 130, 61 (1992).
26. S. Hens, J. Vanhellemont, D. Poelman, P. Clauws, I. Romandic, A. Theuwis, F. Holsteyns, and J. Van Steenbergen, *Appl. Phys. Lett.* 87, 061915 (2005).
27. M. Van Sande, L. Van Goethem, L. De Laet, and H. Guislain, *Appl. Phys. A* 40, 257 (1986).

Publisher's Note Springer Nature remains neutral with regard to jurisdictional claims in published maps and institutional affiliations.